


Thermodynamics of Hygroresponsive Soft Engines: Cycle Analysis and Work Ratio

Beomjune Shin¹, Yeonsu Jung,² Munkyeong Choi¹, and Ho-Young Kim^{1,*}

¹*Department of Mechanical Engineering, Seoul National University, Seoul 08826, Korea*

²*School of Engineering and Applied Sciences, Harvard University, Cambridge, Massachusetts 02138, USA*

 (Received 19 March 2022; revised 27 August 2022; accepted 30 August 2022; published 26 October 2022)

Soft materials that respond to external stimuli, such as moisture, heat, and light, can convert the environmental energy into mechanical motions, and thus can be considered engines. The energy-conversion process within the soft-materials-based engines is fundamentally different from that of conventional heat engines utilizing gaseous media, but has been rarely studied to date. Here we construct a theoretical framework to analyze the thermodynamic performance of humidity-responsive soft actuators, as a canonical model of soft engines, which operate in a similar manner to such motile plants as wild wheat seeds and pine cones. Considering the free-energy change and the work generation through a four-process cycle, we define a work ratio as the work of actual engines relative to that of a so-called hygro-Carnot cycle going through reversible changes of volume and chemical energy. We propose an explanation why natural motile plants exhibit higher work ratios than common artificial hygroscopic actuators based on the time scales of soft actuation and the environmental humidity change. Our thermodynamic model can be extended to a range of soft engines driven by diffusion of stimulus, e.g., solvent, heat, and ions, into soft media.

DOI: [10.1103/PhysRevApplied.18.044061](https://doi.org/10.1103/PhysRevApplied.18.044061)

I. INTRODUCTION

Soft actuators are in general capable of flexible deformation in response to external stimuli including heat, electricity, light, pH, and moisture. Change of molecular structures gives rise to macroscopic deformation by heating in shape memory alloys and polymers [1], and by light absorption in photoresponsive materials (e.g., azobenzene) [2,3]. Ion distribution is localized to produce strains in response to electrical stimulus in electroactive materials [4]. External molecules of solvent like water enter or exit from the polymer network of hydrogels, accompanying volume change, as the temperature [5,6], pH [7,8], or electrical field [9–11] varies. More simply, hygroexpansive materials—such as amorphous cellulose and polyethylene oxide (PEO)—change their volumes by absorbing or losing water molecules in response to the environmental humidity variation [12,13].

Most studies on soft actuators to date have been focused on developing materials or fabrication processes to effectively generate stimulus-responsive strain or stress [14, 15]. Various ingenious motion mechanisms of soft actuators have driven the advance of soft-robotics technology [16,17]. However, mathematical analyses of the dynamic response of those soft actuators have been relatively sparse although the soft robots' optimal design can only be

reached by such a model [18]. The soft-actuation systems can be theoretically understood either from a mechanistic or a thermodynamic point of view. From a mechanistic perspective, the external stimuli lead to internal strains based on diverse mechanisms depending on the material characteristics. The temporal evolution of such strain distribution then should allow us to calculate local stress and global force, torque, and resultant deformation or motion of the soft-actuation system with time [19,20].

As the soft materials directly generate mechanical deformation or motion in response to environmental stimuli, they can be considered as an energy-conversion device just like a generator, a motor, or a heat engine. Most of the soft actuators undergo cyclic deformations to continuously drive soft machines, and thus their thermodynamic energy-conversion efficiency should be of interest to fully utilize available environmental energy. Energy-harvesting technologies have often considered how much electrical energy can be generated out of the environmental energy input [21–24]. However, the thermodynamic cycle analysis of the soft-materials-based engines (referred to as soft engines hereafter), which allows us to calculate the effectiveness of mechanical energy generation through cyclic operation, can seldom be found.

Here, we propose a theoretical framework to analyze the thermodynamic performance of soft engines that directly harness chemical, rather than thermal, energy of the environments. In selecting a particular energy-conversion

*hyk@snu.ac.kr

material and scheme, we pay attention to a motion generation strategy adopted by such plants as pine cones [Fig. 1(a)] [25], wild wheats [26], and seeds of *Erodium* [27] and *Pelargonium* [28,29] species. Those botanical actuators are commonly composed of bilayers, one of whose layers is hygroexpansive and the other not. The environmental humidity change induces diffusion of water molecules into or out of the hygroexpansive tissue, whose local volume change leads to global deformation of the bilayer. We consider both natural and artificial hygroresponsive actuators in this work. Our theoretical model can be easily generalized for a variety of soft actuators driven by diffusion of environmental stimuli including solvent [30,31], heat [32,33], and ions [34].

In the following, we start with briefly describing the structure and properties of our artificial actuator that emulates the hygroresponsive motions of the aforementioned motile plants. After reviewing the mechanistic theory to predict the dynamics of actuator response, we construct thermodynamic models to analyze the energy-conversion process of the hygroexpansive soft engines. Then we present a concept of work ratio that allows us to evaluate the thermodynamic performance of natural and artificial soft actuators. We finally discuss design strategies of these actuators depending on the characteristic time scales of environmental humidity change.

II. RESULTS

A. Hygroresponsive actuators

As a humidity-responsive material for soft actuation, we select PEO for its superior hygroexpansivity, low toxicity, and ease of electrospinning [35]. We employ the directional electrospinning process to obtain aligned nanofibrous sheets of PEO, which ensure fast diffusion of water vapor owing to its high porosity, and a large degree of elongation in the fiber direction. Figure 1(b) shows a SEM image of the fabricated PEO sheet. We measure various mechanical properties of the sheet, such as the density, porosity, hygroexpansion coefficient α_h , and Young's modulus E , which are listed in Table I.

Many hygroscopic botanical actuators, including pine cones and wild wheats, have bilayer structures, such that one layer is hygroexpansive while the other is hygroscopically inactive, to function in a similar fashion to bimetallic strips [36]. Following this tactic, we made a hygroresponsive bilayer actuator by attaching a sticky, hygroscopically inactive polyimide (PI) tape to the PEO fibrous sheet. The bilayer can bend in response to environmental humidity change [Fig. 1(c)], whose dynamics can be predicted using a theory developed by Shin *et al.* [37]. We briefly delineate the theory as it serves as a basis for the subsequent thermodynamic modeling of the soft machines driven by those actuators.

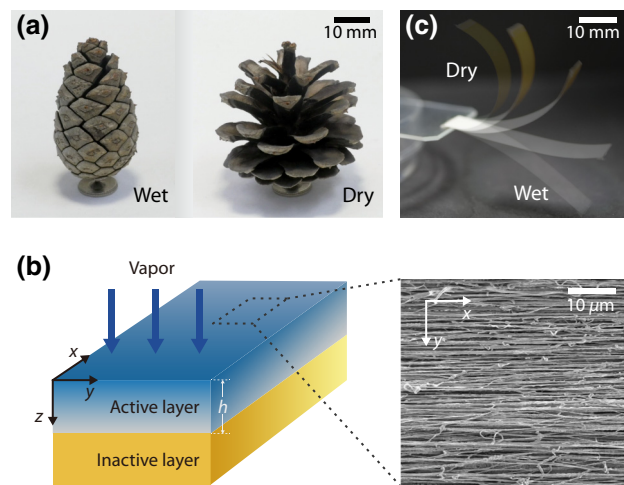


FIG. 1. (a) The scales of pine cone are opened as the surrounding air gets dry. (b) The active layer of actuator is composed of unidirectionally aligned nanofibers, which expand by absorbing water molecules. The scanning electron micrograph shows nanofibrous structure of the electrospun active layer. (c) The actuator mimicking the movement of plants repeats bending and unbending in response to periodic humidity change.

As the surrounding humidity increases from an initial dry state, the water molecules diffuse into the active layer, so that the water concentration $\phi(z, t)$ follows the one-dimensional unsteady diffusion equation: $\partial\phi/\partial t = D\partial^2\phi/\partial z^2$, where t is time and D is the diffusion coefficient of vapor in the active layer. The coordinate system is shown in Fig. 1(b). The boundary conditions are given as $\phi(0, t) = \phi_\infty$ at the outer surface exposed to the surrounding air of humidity ϕ_∞ , and as $\partial\phi(h, t)/\partial z = 0$ at the interface of the active and inactive layer. Combined with the initial condition of $\phi(z, 0) = \phi_0$ with ϕ_0 being the initial concentration, the diffusion equation is solved to give

$$\phi(z, t) = \sum_{n=1}^{\infty} \left[\frac{-2(\phi_0 - \phi_\infty)}{(n + 1/2)\pi} e^{-\gamma_n^2 t} \sin \frac{(n + 1/2)\pi z}{h} \right] + \phi_\infty, \quad (1)$$

where $\gamma_n = D^{1/2}(n + 1/2)\pi/h$.

TABLE I. Mechanical properties of the directionally electrospun nanofibrous sheet of PEO. The hygroexpansion coefficient refers to the strain increase per 1% of relative humidity increase at room temperature. In Young's modulus, ϕ denotes the relative humidity. The hygroexpansion coefficient and Young's modulus are measured in the fiber-alignment direction [x axis in Fig. 1(b)].

Density (kg/m ³)	1125
Porosity	0.7
Hygroexpansion coefficient	0.051
Young's modulus (MPa)	$-77.4\phi + 169.2$

The spatial distribution of water concentration induces the hygroscopic strain in the active layer, which eventually causes bending of the actuator. The total strain in the active layer is given by $\epsilon(z, t) = \epsilon_0 - \kappa\zeta - \epsilon_h$, where ϵ_0 is the reference strain in the reference plane (taken as the plane farthest from the center of curvature), ζ the distance from the reference plane, κ the bending curvature, and $\epsilon_h = \alpha_h\phi$ the hygroscopic strain. Integrating the local stress $\sigma = E\epsilon$, we obtain the bending force $F = \int \sigma d\zeta$ and the bending moment $M = \int \sigma\zeta d\zeta$. In the absence of the external loads, we write $F = A\epsilon_0 - B\kappa - F_\alpha = 0$ and $M = B\epsilon_0 - D\kappa - M_\alpha = 0$ for the bilayer, where $A = \int E d\zeta$, $B = \int E\zeta d\zeta$, $D = \int E\zeta^2 d\zeta$, $F_\alpha = \int E\epsilon_h d\zeta$, and $M_\alpha = \int E\epsilon_h\zeta d\zeta$. As a result, the curvature becomes

$$\kappa = \frac{AM_\alpha - BF_\alpha}{B^2 - AD}. \quad (2)$$

Numerical integration of Eq. (2) combined with the distribution of ϕ from Eq. (1) gives the curvature as a function of time. The model is experimentally shown to accurately predict the temporal curvature change of the bilayers having various thicknesses [37].

B. Thermodynamic cycle analysis of hygroexpansive soft engines

A soft actuator, in general, changes its shape when subjected to energy input (or stimulus) from the surroundings, and returns to its initial state with the removal of the external stimulus. Repetitive supply and deprivation of the stimulus results in cyclic operation of the soft actuator, which naturally raises a question of how much available energy is converted to mechanical work. Although classical thermodynamic analyses [38] have answered such a question for energy-conversion devices involving heat transfer (due to temperature difference between the system and the surroundings), they cannot be directly applied to soft engines, which use neither heat input as an energy source nor gas as a working medium. Thus, here we construct a theoretical framework to analyze the thermodynamic cycle of hygroexpansive soft engines that harness environmental humidity energy. To this end, we need to idealize the cyclic process of soft actuation just as was done for conventional heat engines.

We begin with the classical Carnot cycle, an ideal cycle that runs between two thermal reservoirs, as an inspiration for our idealized cycle of soft engines. As shown in Fig. 2(a), the gas, the working medium of the Carnot cycle, is compressed while being thermally insulated, so that its temperature rises from that of the cold reservoir T_c to that of the hot reservoir T_h (reversible adiabatic compression) in process 1 (stage 1 to 2). In process 2 (stage 2 to 3), the gas expands as heat is transferred from the hot reservoir. During this process, the temperature does not change while the gas does work on the surroundings (isothermal

expansion). In process 3 (stage 3 to 4), the gas continues to expand while being thermally insulated, so that its temperature drops from T_h to T_c (reversible adiabatic expansion). In process 4 (stage 4 to 1), the gas is compressed while keeping the same temperature as the cold reservoir, so that the surroundings do work on the gas (isothermal compression). Thanks to frictionless piston motion and reversible heat transfer, the Carnot heat engine exhibits the maximum efficiency possible between two thermal reservoirs at T_h and T_c . The work done by the system (gas) to the surroundings, W is given by $W = Q_h - Q_c$ by the first law of thermodynamics with Q_h being the thermal energy transferred from the hot reservoir to the system and Q_c the thermal energy transferred from the system to the cold reservoir. Because $Q_h = T_h\Delta S$ and $Q_c = T_c\Delta S$, where ΔS is the entropy difference between stages 2 and 3 (or 4 and 1), we get the thermodynamic efficiency $\eta = W/Q_h = 1 - T_c/T_h$.

C. Isotropic soft engines

Now we theoretically construct an ideal isotropic humidity-responsive soft-engine cycle, which runs between two humidity (rather than thermal) reservoirs under isothermal condition. Just as the Carnot engine does work to the surroundings by expansion owing to heat transfer from the surroundings, the ideal isotropic soft engine does work by changing its volume owing to moisture transfer from the surroundings. The system is compressed doing negative work to the surroundings as losing heat in the Carnot engine and losing moisture in the ideal isotropic soft engine.

As the internal energy changes due to heat transfer and mechanical work in thermal engines, the free-energy changes due to moisture transfer and mechanical work in hygro-soft engines. Following Flory and Rehner [39], we describe the free-energy density F associated with hygroscopic swelling of polymers as a sum of contributions due to mixing (F_m) and stretching (F_s): $F = F_m + F_s$, where $F_m = k_B T [(J-1) \ln(1-1/J) + \chi(1-1/J)] / \Omega_f$ and $F_s = k_B T (\lambda_x^2 + \lambda_y^2 + \lambda_z^2 - 3 - 2 \ln J) / (2\Omega_p)$. Here, k_B is the Boltzmann constant, T is temperature of the system, Ω_f is the volume of a water molecule, Ω_p is the volume of a polymer molecule in the dry state, λ_i is the stretch (ratio of the elongated length to the original length) along the i th principal axis, $J = \lambda_x\lambda_y\lambda_z$ is the relative volume change of deformation, and χ is the Flory-Huggins interaction parameter. The change of free energy is written as $dF = dL + dW$, where $dL = \mu\Omega_f^{-1}dJ$ and $dW = \sigma_i d\lambda_i$, respectively, account for chemical energy and mechanical work. Under the incompressibility constraint, the change in volume of the polymer corresponds to the volume of the absorbed solvent. Here we note that the positive work signifies the work done by the surroundings to the system.

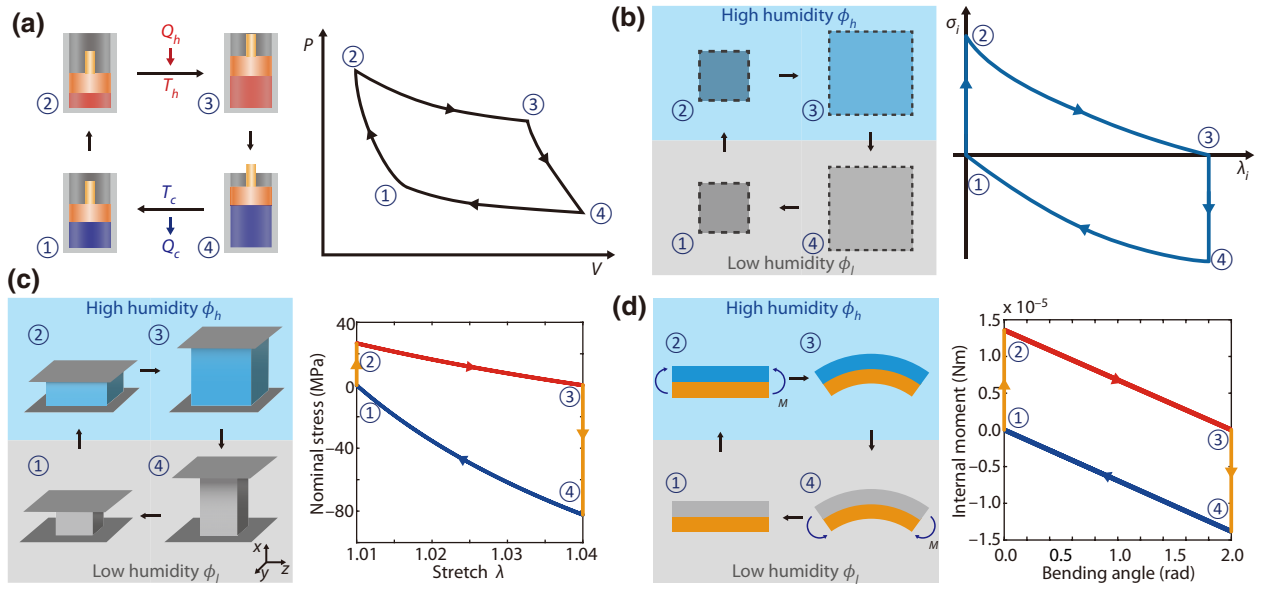


FIG. 2. (a) Schematics and the pressure (P)–volume (V) diagram of Carnot cycle for heat engines. Schematics of the cyclic operation and state diagram of (b) the isotropic soft engine, (c) the unireciprocal soft engine, and (d) the bending soft engine.

The isotropic engine consists of two adiabatic and two isochemical potential processes, similar to the Carnot engine having two adiabatic and two isothermal processes. We assume that the soft material (hygroexpansive polymer) and the surroundings are in thermal and chemical equilibrium all the time, making the water transport a reversible process. The chemical equilibrium signifies the equal chemical potential of the polymer and of the surroundings at the relative humidity of ϕ , so that we get $\mu = \mu^0 + k_B T \ln \phi$ all the time. Here, μ^0 represents the standard chemical potential of water. Figure 2(b) schematically describes the ideal hygroresponsive engine with the stress (σ_i)–stretch (λ_i) diagram. Each process is delineated as the following.

(1) Adiabatic, chemical potential growth process (state 1 to 2): the relative humidity of the surroundings is increased from ϕ_l to ϕ_h , increasing the chemical potential of the system. Because no water molecules are transported across the boundary (adiabatic), the volume does not change, leading to $\Delta F_{12} = \Delta L_{12} + \Delta W_{12} = 0$. As the chemical potential, μ increases with the surrounding relative humidity, so does the stress despite constant volume.

(2) Isochemical potential, expansion process (state 2 to 3): the polymer swells isotropically by absorbing water molecules from the surroundings of a constant high relative humidity (ϕ_h). Because the chemical potential is fixed at $\mu_h = \mu^0 + k_B T \ln \phi_h$, the chemical energy transferred to the polymer can be written as $\Delta L_{23} = \mu_h \Omega_f^{-1} \Delta J_{23}$ with the volume change of ΔJ_{23} . Then the mechanical work is given by the difference of the free-energy change and the transferred chemical energy during this process, or $\Delta W_{23} = \Delta F_{23} - \mu_h \Omega_f^{-1} \Delta J_{23}$.

(3) Adiabatic, chemical potential decrease process (state 3 to 4): the relative humidity of the surroundings is decreased from ϕ_h to ϕ_l , leading to decrease of the chemical potential of the system. Because no water molecules are transported across the boundary (adiabatic), changes in volume and free energy of the system are zero. Thus, we have $\Delta F_{34} = \Delta L_{34} + \Delta W_{34} = 0$. As the chemical potential μ decreases with the surrounding relative humidity, so does the stress despite constant volume.

(4) Isochemical potential, compression process (state 4 to 1): the polymer shrinks by losing water molecules to the surroundings of constant low humidity (ϕ_l). Similar to process 2, the mechanical work during the process is given by $\Delta W_{41} = \Delta F_{41} - \mu_l \Omega_f^{-1} \Delta J_{41}$. The net mechanical work generated through one cycle, W_{net} is a sum of the mechanical work arising in processes 2 and 4, and thus $W_{\text{net}} = \Delta W_{23} + \Delta W_{41}$. Because there should be no changes in free energy and volume upon completion of cycle, we write $\Delta F_{23} + \Delta F_{41} = 0$ and $\Delta J_{23} + \Delta J_{41} = 0$. Then it follows that $W_{\text{net}} = (\mu_l - \mu_h) \Omega_f^{-1} \Delta J_{23}$ as $\Delta J_{23} = -\Delta J_{41}$. We find $W_{\text{net}} < 0$ because $\mu_l < \mu_h$ and $\Delta J_{23} > 0$, meaning that the system does net work to the surroundings during the cycle. We define the net mechanical work (W_{net}) produced within the isotropic soft engine as the maximum extractable work (W_{max}) of a given soft material operated within a specific humidity range. The amount of chemical energy transfer in processes 2 and 4 are, respectively, $\Delta L_{23} = \mu_h \Omega_f^{-1} \Delta J_{23} < 0$ and $\Delta L_{41} = \mu_l \Omega_f^{-1} \Delta J_{41} > 0$.

Defining the efficiency as the ratio of the net work (W_{net}) to the positive input of chemical energy ($L_{\text{in}} = \Delta L_{41}$) in an analogous manner to the Carnot cycle, we get $\eta = W_{\text{net}}/L_{\text{in}} = 1 - \mu_h/\mu_l$. We thus see that the efficiency of

the ideal hygroresponsive cycle is determined only by the ratio of the chemical potentials, represented as a function of relative humidity, of surroundings. For example, if the cycle operates between the relative humidity of $\phi_h = 0.8$ and $\phi_l = 0.2$, the efficiency is calculated to be 86% with the standard chemical potential, μ^0 taken to be zero.

A remarkable difference between the isotropic soft engine from the conventional Carnot heat engine is that the soft engine does work to the surroundings during both expansion (from stage 2 to 3) and compression (from stage 4 to 1). The heat engine does work to the surroundings only during expansion (from stage 2 to 4) while the surroundings do work to the system during compression (from stage 4 to 2). The working medium of the heat engine, gas, is always under the positive pressure [P in Fig. 2(a) is always positive], so that the direction of volume change, either compression or expansion, determines the sign of the work. On the other hand, the working medium of the hygroresponsive engine, a soft solid, changes the sign of its stress depending on the direction of volume change [σ_x is positive during expansion and negative during compression in Fig. 2(b)], so that the work done to the system is always negative (or the work done to the surroundings is always positive).

D. Unireciprocal soft engines

Because most soft engines push or bend the surrounding mechanical structures in a designated direction to generate useful work, here we analyze the thermodynamic cycle of such an engine. In heat engines, the pressure in the gas is scalar, and thus a simple piston motion in Fig. 2(a) can represent general volume expansion. But a soft engine, whose motion is directionally restricted, works differently from the above ideal soft engine employing isotropic expansion of the soft solid. We first consider an idealized soft engine as shown in Fig. 2(c), which pushes an imaginary movable solid boundary in one direction (x) and allows the solid to freely expand in the other directions (y and z). We refer to such an engine as an unireciprocal (able to make useful work reciprocally in one axis) engine. We analyze this type of soft-engine cycle by replacing the two adiabatic processes above by the constant x -stroke processes.

(1) Constant x -stroke, absorption process (state 1 to 2): the relative humidity of the surroundings is increased from ϕ_l to ϕ_h , increasing the chemical potential of the system. The soft medium absorbs water molecules, and is allowed to freely expand in the y and z directions without deformation in the x direction. The x -directional stress is given by $\sigma_x = Nk_B T(\lambda_x - \lambda_x^{-1}) - \Pi\lambda_y\lambda_z$, where the osmotic pressure $\Pi = \mu/\Omega_f - k_B T[\ln(1 - 1/J) + 1/J + \chi/J^2]/\Omega_f$ [40]. The stress increases with absorption, and Fig. 2(c) shows the stress (σ)–stretch (λ) diagram. Although the mechanical work ΔW_{12} is zero, the chemical energy transferred from the surroundings to the system is

given by $\Delta L_{12} = \int \mu\Omega_f^{-1} dJ_{12} < 0$, implying that the free energy is decreased in this process: $\Delta F_{12} = \Delta L_{12} < 0$.

(2) Isochemical potential, expansion process (state 2 to 3): the medium swells in the x direction to push the boundary (doing work to the surroundings) by absorbing water molecules from the surroundings of a constant high relative humidity (ϕ_h). The stretch in the y and z directions is fixed. Because the chemical potential is fixed at μ_h , the chemical energy transferred to the medium can be written as $\Delta L_{23} = \mu_h\Omega_f^{-1}\Delta J_{23}$ with the volume change of ΔJ_{23} . The mechanical work is given by $\Delta W_{23} = \int \sigma_x d\lambda_x$.

(3) Constant x -stroke, desorption process (state 3 to 4): the relative humidity of the surroundings is decreased from ϕ_h to ϕ_l , decreasing the chemical potential of the system. The medium contracts in the y and z directions with no stress because it loses water to the surroundings while maintaining a constant stroke in the x -direction. The x -directional stress turns to negative (compressive) and its magnitude increases during the process. Although the mechanical work ΔW_{34} is zero, the chemical energy transferred from the surroundings to the system is given by $\Delta L_{34} = \int \mu\Omega_f^{-1} dJ_{34} > 0$, implying that the free energy is increased in this process: $\Delta F_{34} = \Delta L_{34} > 0$.

(4) Isochemical potential, compression process (state 4 to 1): the medium shrinks in the x direction to pull the boundary by losing water molecules to the surroundings of a constant low relative humidity (ϕ_l). The stretch in the y and z directions are fixed. Because the chemical potential is fixed at μ_l , the chemical energy transferred to the system can be written as $\Delta L_{41} = \mu_l\Omega_f^{-1}\Delta J_{41}$ with the volume change of ΔJ_{41} . The mechanical work is given by $W_{41} = \int \sigma_x d\lambda_x$.

To obtain the thermodynamic efficiency of this soft engine, we note that the net work $W_{\text{net}} = \Delta W_{23} + \Delta W_{41}$ should be equal to $L_{\text{in}} - L_{\text{out}}$ because the net free-energy change is zero after a cycle. The chemical energy input L_{in} corresponds to $L_{\text{in}} = \Delta L_{34} + \Delta L_{41}$, and the output $L_{\text{out}} = \Delta L_{12} + \Delta L_{23}$. While the above isotropic engine allows simple evaluation of L_{in} and L_{out} using the constant relative humidities, we resort to the following relationships in this case for difficulties in integrating the chemical potential in processes 1 and 3: $L_{\text{in}} = \Delta F_{31} - \Delta W_{41}$ and $L_{\text{out}} = \Delta F_{13} - \Delta W_{23}$, where F and W can be obtained using the stretch at each state and Flory-Huggins interaction parameter χ of the soft solid. We can empirically find χ for a polymer by letting $\sigma = 0$ in a freely swollen state of polymer with a known value of stretch.

With the idealized cycle given above, now we present how to evaluate the efficiency of an imaginary unireciprocal engine made of directionally electrospun PEO as prepared in this work. We find $\chi = 0.995$ for a stress-free state in a relatively dry environment ($\phi_l = 0.2$, $\lambda_l = 1.01$, $J = 1.03$) and $\chi = 1.37$ for a stress-free state in a relatively humid environment ($\phi_h = 0.8$, $\lambda_h = 1.04$,

$J = 1.13$). We write $\Omega_f = 2.99 \times 10^{-29} \text{ m}^3$ and $\Omega_p = 4.43 \times 10^{-25} \text{ m}^3$ using the molecular weight and density of water and PEO, respectively. Then we obtain $\Delta W_{23} = 3.7 \times 10^{-4} \text{ J}$, $\Delta W_{41} = 1.42 \times 10^{-3} \text{ J}$, and $W_{\text{net}} = 1.79 \times 10^{-3} \text{ J}$ for a sample sized $1 \times 1 \times 1 \text{ mm}^3$. The chemical energy input per cycle is $L_{\text{in}} = 7.6 \times 10^{-3} \text{ J}$, and the efficiency $\eta = W_{\text{net}}/L_{\text{in}}$ is found to be 23.6%. The major difference between isotropic engine and unireciprocal engine is whether to allow expansion in the y and z directions when the surrounding chemical potential is changed. During processes (1) and (3) of unireciprocal engine, the water molecules are transported without generating mechanical work, which mainly accounts for the reduction of the net work and efficiency.

E. Bending soft engines

We now consider a phytomimetic bilayer actuator as fabricated in this work, which repeats bending and unbending under a cyclic change of environmental humidity. While the above soft engines involve the active material alone, the bending soft engine involves an inactive layer that should deform passively following the active layer. For the ideal thermodynamic cycle of the bending engine as shown in Fig. 2(d), we construct a diagram of the internal moment versus the bending angle of the bilayer.

(1) Constant bending angle, chemical potential growth process (state 1 to 2): the relative humidity of the surroundings is increased from ϕ_l to ϕ_h , increasing the chemical potential of the system. The active layer absorbing water molecules is prevented from deforming by an internal moment, M , which increases during process 1. The mechanical work ΔW_{12} and transferred chemical energy ΔL_{12} are zero because of constant bending angle of the bilayer. The free-energy change becomes $\Delta F_{12} = \Delta L_{12} + \Delta W_{12} = 0$.

(2) Isochemical potential, bending process (state 2 to 3): the bilayer bends as the internal moment is relieved while keeping the identical chemical potential to the humid surroundings. The chemical energy transferred to the active layer $\Delta L_{23} = \mu_h \Omega_f^{-1} \Delta J_{23}$. The molecular incompressibility constraint allows us to calculate the number of water molecules involved in this process, $\Omega_f^{-1} \Delta J_{23}$ with the volumetric expansion induced by the bilayer bending. The difference between the volume of the active layer of states 2 and 3 is written as $\theta h w / 2$ with the bending angle θ , the thickness of active layer h , and the width of the actuator w . The mechanical work, ΔW_{23} becomes $\Delta W_{23} = \int M d\theta$, where $M = M_{\text{max}} - \Sigma E_j I_j \theta / L$. Here, E_j and I_j are, respectively, Young's modulus and the area moment of inertia of the j th layer (ranging from the active to the inactive layer), and L is the actuator length.

(3) Constant bending angle, chemical potential decrease process (state 3 to 4): the relative humidity of the surroundings is decreased from ϕ_h to ϕ_l , decreasing the chemical

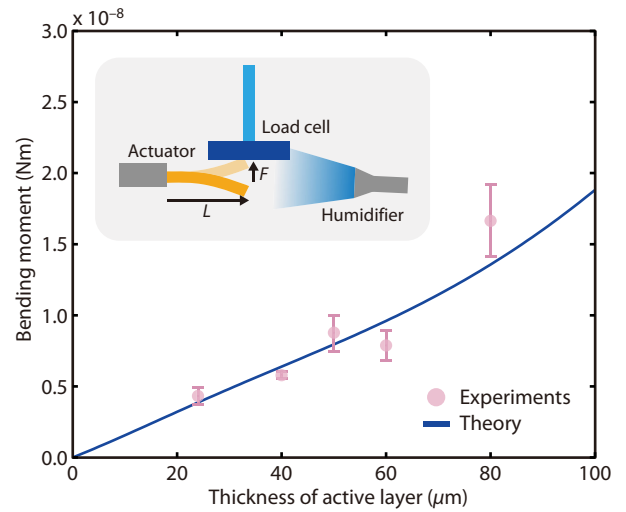


FIG. 3. The experimental data and theoretical predictions of the bending moment of the bilayer actuator as a function of the active layer thickness. Inset, schematic of the experimental setup to measure the bending moment, FL , where F is the force acting on the load cell by the tip of the actuator.

potential of the system. The active layer losing water molecules is prevented from deforming by an internal moment, whose magnitude grows during the process.

(4) Isochemical potential, unbending process (state 4 to 1): the bilayer unbends reversibly as the internal moment is relieved while keeping the identical chemical potential to the surroundings of a low humidity. In a real system, we can experimentally find ΔW_{41} as $\Delta W_{41} = \int M d\theta$, where $M = M_{\text{max}} - \Sigma E_j I_j \theta / L$.

With the idealized cycle given above, we now discuss how to experimentally measure the work generated by actual bilayer actuators composed of the directionally electrospun PEO active layer and the PI inactive layer. Figure 3 shows the maximum bending moment, M_{max} , as a function of the thickness of active PEO layer with the humidity varying from $\phi_l = 0.3$ to $\phi_h = 0.8$. The inactive layer thickness is $30 \mu\text{m}$, the width and length of the bilayer actuator is 5 and 20 mm, respectively. The theoretical values of bending moment is consistent with the experimental values measured by sensing the force generated at the bilayer tip. For an actuator with the active layer $30 \mu\text{m}$ thick, integrating the moment with respect to the bending angle gives $W_{\text{net}} = \Delta W_{23} + \Delta W_{41} = 2.26 \times 10^{-5} \text{ J}$. The thermodynamic efficiency of the bending soft engine is now calculated to be $\eta = W_{\text{net}}/L_{\text{in}} = 1.15\%$ with $L_{\text{in}} = 1.97 \times 10^{-3} \text{ J}$. The bending soft engine exhibits a lower efficiency than the above unireciprocal engine mainly because of the inactive layer restraining the deformation of the active layer.

Now a question may arise naturally why so many motile plants have adopted bending bilayer structures of a low thermodynamic efficiency rather than other schemes

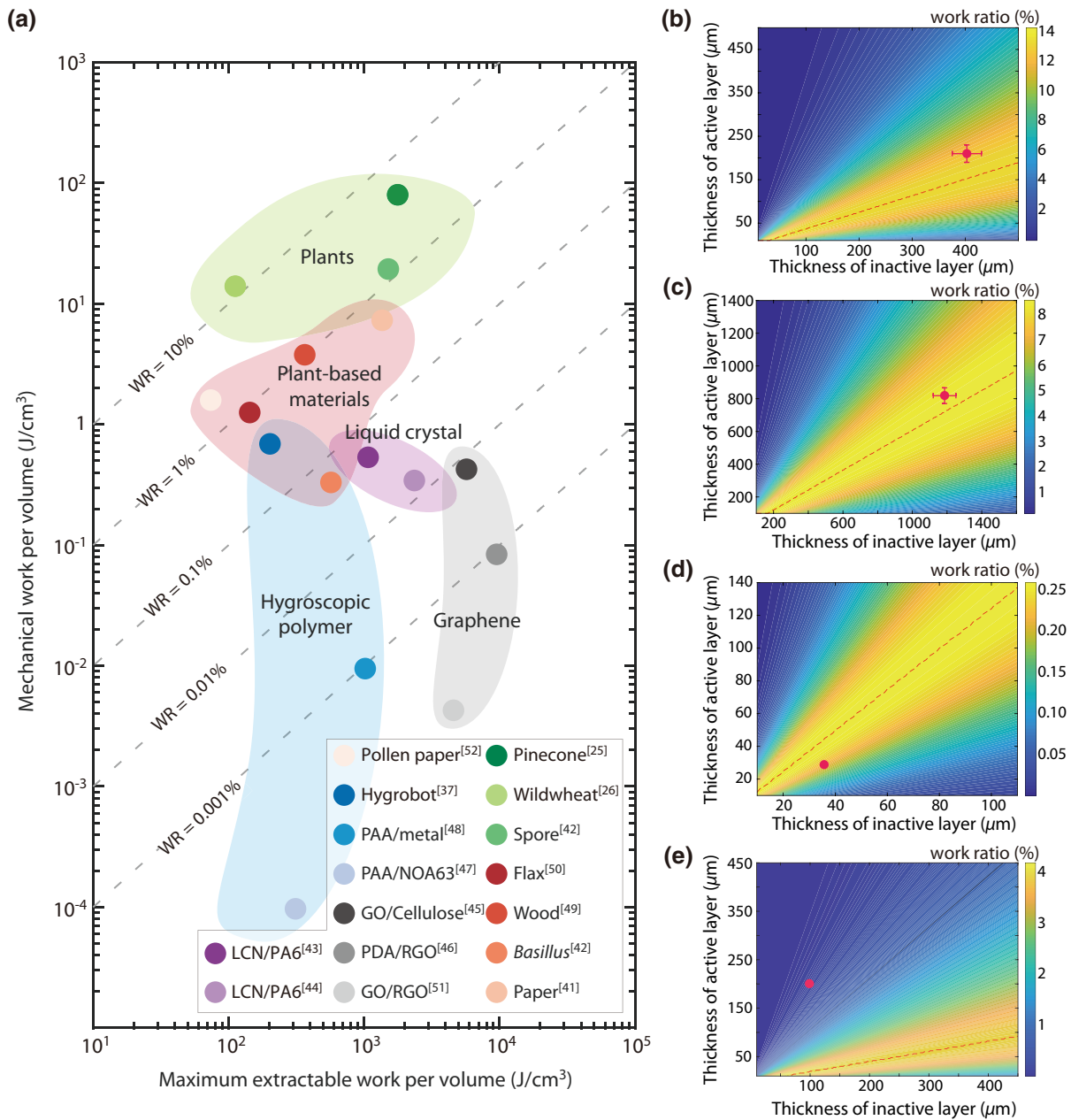


FIG. 4. (a) Work ratio (WR) of various soft engines including natural plants and artificial actuators. The contour map of work ratios of (b) seed of wild wheat [26], (c) pine cone [25], (d) artificial hygrobot [37], and (e) paper-polymer bilayer [41]. Red circles indicate the dimension of each actuator. Abbreviations of materials in the legend of (a) are given in Table S2 in the Supplemental Material [53]. The data points were calculated using values from [25,26,37,41–52].

including unireciprocal structure of a high efficiency. An obvious explanation comes from the fact that the actuation distance achieved by bending is much greater than by expansion. For example, the mere stretching of PEO layer in the high humidity of 80% allows the tip of the actuator to reach approximately 5% farther than the original dry length. However, the bilayer structure fabricated in this work allows the tip of the actuator to swing a distance comparable to the original dry length.

F. Work ratio

Here we develop a measure to compare the performance of various natural and artificial soft bending actuators reported to date [25,26,37,41–52]. Although the theoretical framework constructed above allows us to calculate the thermodynamic efficiency of soft engines, it tends to monotonically increase as the active layer thickness decreases even in the expense of the magnitude of mechanical work, as discussed in Sec. S1 of Supplemental

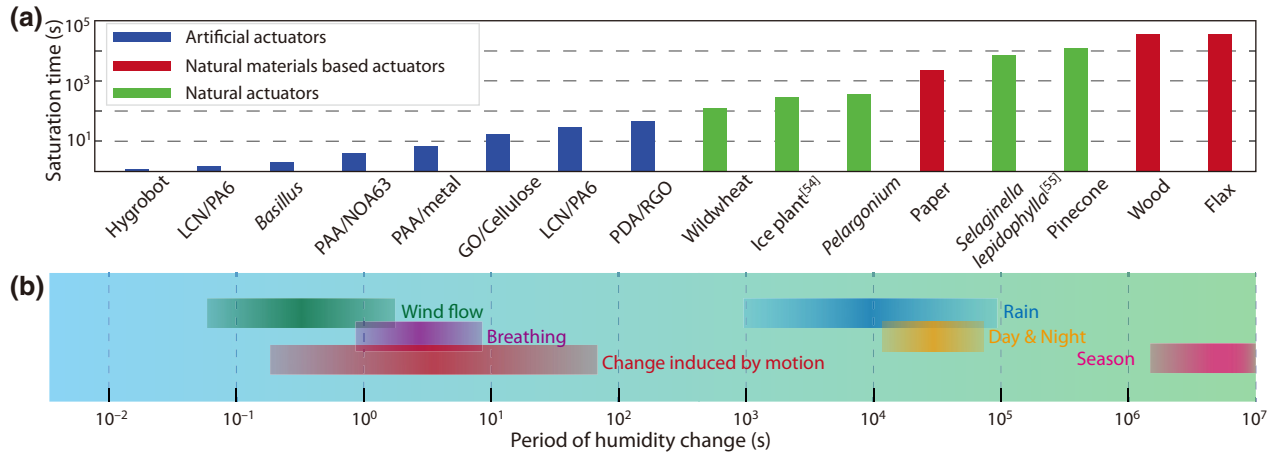


FIG. 5. (a) Characteristic operation times, or saturation times, of various hygroscopic soft engines. (b) Periods of humidity change due to various causes, which can be harnessed by natural and artificial soft actuators.

Material [53]. Thus, the efficiency cannot reflect the effectiveness of the soft actuators that need to generate as much work as possible under a given condition. Therefore, we introduce a work ratio, Γ , defined as $\Gamma = W_{\text{net}}/W_{\text{max}}$, as a suitable measure for the work generation effectiveness of bending soft actuators. Here, W_{max} is the maximum extractable work of a given soft medium going through an ideal isotropic (hygro-Carnot) cycle. Thus, we get $W_{\text{max}} = -(\mu_l - \mu_h)\Omega_f^{-1}\Delta J_{\text{max}}$ with ΔJ_{max} being the maximum ratio of water volume expansion. The net work generated by the bending cycle is given by $W_{\text{net}} = \Sigma E_j I_j \kappa_{\text{max}}^2$. The experimental validation for the theoretical prediction of work ratio is discussed in Sec. S2 of Supplemental Material [53].

Upon gathering information of the dimensions and Young's moduli of active and inactive layers of various hygroresponsive soft actuators available in the literature (Table S1 in the Supplemental Material [53]), we plot W_{net} versus W_{max} in Fig. 4(a). We see that the natural actuators, including pine cones, wild wheats, and *Bacillus* spores, have relatively high work ratios ranging from approximately 0.2 to 2% while the artificial actuators possess relatively low work ratios. Among the artificial actuators, those using plant-based materials including pollen, wood, and flax have relatively high work ratios.

For bending soft engines, the functional dependence of work ratio can be estimated as

$$\Gamma \sim \frac{\Sigma E_j I_j \kappa_{\text{max}}^2}{\alpha_h \Delta \phi \Delta \mu} \sim \frac{\Sigma E_j I_j \alpha_h \Delta \phi f^2(m, n)}{\Delta \mu}, \quad (3)$$

where κ_{max} is the maximum change in curvature, $\kappa_{\text{max}} = \alpha_h \Delta \phi f(m, n)$. The design factor, $f(m, n)$ is given by [41]

$$f(m, n) = \frac{1}{h_t} \frac{6(1+m)^2}{3(1+m)^2 + (1+mn)[m^2 + 1/(mn)]}, \quad (4)$$

where h_t is the total bilayer thickness, m is the ratio of the active layer thickness to the inactive layer thickness, and n is the ratio of Young's modulus of the active layer to the inactive layer. Under a given humidity range $\Delta \phi$, the work ratio improves with the increase of such material properties as the hygroexpansion coefficient α_h of the active layer and Young's moduli of the active and inactive layers. The design factor, $f(m, n)$ plays a critical role in determining the work ratio of the engines made up of the same combination of materials. Figures 4(b)–4(e) plot the work ratio as a function of the thicknesses of active and inactive layers, where the optimal thickness ratio yielding the maximum Γ is denoted by a red dashed line. Plants, Figs. 4(b) and 4(c), have in general relatively high Γ thanks to their high elastic modulus and the actual dimension being rather close to the optimal line. On the other hand, artificial actuators usually aimed to achieve high actuation speed rather than high work ratio, Figs. 4(d) and 4(e), have relatively low Γ because of low elastic modulus (d) or the dimensions being relatively far from the optimal line (b).

III. DISCUSSION

Upon the basis of our mechanistic model for the temporal evolution of the bending curvature and thermodynamic model for the work ratio of bilayer actuators, we now discuss the design strategy suitable for the artificial and natural soft hygroscopic actuators. As the active layer in the bilayer is driven by diffusion of humidity, which takes a finite time, a critical factor in design is the balance between the period of environmental humidity change and the layer's characteristic response time. For example, if one harnesses a very slowly changing humidity condition, the actuator can fully exploit the hygroexpansivity of the active material without needing fast response. In contrast, if one exploits a fast-changing humidity as a power source, the actuator should be designed to keep up with the rate of

humidity variation. Figure 5(a) shows the saturation time, τ , of artificial and natural hygroscopic bilayer actuators available in the literature [25,26,28,37,41–50,54,55]. Saturation of active materials is achieved by humidity diffusion having the time scale of $\tau = h^2/D$ with h being the active layer thickness and D the vapor diffusivity, which corresponds to the characteristic response time of the actuator to the environmental humidity change, as seen in Eq. (1). We see that natural actuators of plants and natural-materials-based actuators used for architecture have relatively long response times while the artificial actuators have short response times.

Figure 5(b) shows the time scales of humidity change due to various causes, including seasonal change (dry winter and humid summer), day–night change, intermittent rain, and breathing. Comparing Figs. 5(a) and 5(b) allows us to figure out the distinctive design strategies, or saturation times of active layers, of the natural and the artificial actuators, as delineated in the following.

Wild wheat seeds bend their awns to propel themselves into soil for germination, which harnesses the humidity variation between day and night [26]. Pine cones open to disperse seeds as a dry season comes [25]. Such botanical movements are driven by long periods of humidity change, ranging from 10^4 to 10^7 s. Therefore, those plants do not need to shorten the diffusion time by reducing the active layer thickness or using a high-diffusivity material, which can potentially sacrifice the stiffness. Being free from constraint of response speed, the botanical actuators can be designed in such a way that the bending work under a given humidity condition may be maximized to effectively achieve their goals of either propulsion or seed dispersal, which would eventually maximize the probability of reproduction [56,57].

Artificial actuators are commonly designed to harness relatively fast humidity variation caused by breathing, wind flow, or oscillation of the actuators themselves between humid and dry regions. Therefore, the active layers must be thin (small h) and highly diffusive (high D) to easily demonstrate the performance of the actuators. As a result, the work ratios of the relatively fast artificial actuators tend to be much lower than the slow natural actuators.

In summary, we construct a theoretical framework to analyze the thermodynamic performance of humidity-responsive soft engines. We show that four-process cycle models allow us to obtain the free-energy change and work generation associated with the cyclic operation of the soft actuators. We use a work ratio, defined as the work of an actual soft engine relative to that of a so-called hygro-Carnot cycle going through reversible changes of volume and chemical energy, in order to evaluate the effectiveness of natural and artificial actuators from the thermodynamic point of view. By comparing the time scales of humidity changes due to various causes, we propose an explanation

why the slowly responding natural actuators are designed to have a higher work ratio than the fast artificial actuators. The mechanistic and thermodynamic models through this work can be applied to other soft engines driven by diffusion of such stimuli as solvents, heat, and ions.

ACKNOWLEDGMENTS

We are grateful to Professor H.H. Song for helpful discussion. This work is supported by the National Research Foundation of Korea (Grant No. 2018-052541) via SNU-IAMD.

-
- [1] W.-S. Ko, S. B. Maisel, B. Grabowski, J. B. Jeon, and J. Neugebauer, Atomic scale processes of phase transformations in nanocrystalline NiTi shape-memory alloys, *Acta Mater.* **123**, 90 (2017).
 - [2] C. J. Barrett, J.-i. Mamiya, K. G. Yager, and T. Ikeda, Photo-mechanical effects in azobenzene-containing soft materials, *Soft Matter* **3**, 1249 (2007).
 - [3] Y. Hao, S. Huang, Y. Guo, L. Zhou, H. Hao, C. J. Barrett, and H. Yu, Photoinduced multi-directional deformation of azobenzene molecular crystals, *J. Mater. Chem. C* **7**, 503 (2019).
 - [4] D. Morales, E. Palleau, M. D. Dickey, and O. D. Velev, Electro-actuated hydrogel walkers with dual responsive legs, *Soft Matter* **10**, 1337 (2014).
 - [5] R. Yoshida, K. Uchida, Y. Kaneko, K. Sakai, A. Kikuchi, Y. Sakurai, and T. Okano, Comb-type grafted hydrogels with rapid deswelling response to temperature changes, *Nature* **374**, 240 (1995).
 - [6] V. Magdanz, G. Stoychev, L. Ionov, S. Sanchez, and O. G. Schmidt, Stimuli-responsive microjets with reconfigurable shape, *Angew. Chem.* **126**, 2711 (2014).
 - [7] A. Shastri, L. M. McGregor, Y. Liu, V. Harris, H. Nan, M. Mujica, Y. Vasquez, A. Bhattacharya, Y. Ma, M. Aizenberg, O. Kuksenok, A. C. Balazs, J. Aizenberg, and X. He, An aptamer-functionalized chemomechanically modulated biomolecule catch-and-release system, *Nat. Chem.* **7**, 447 (2015).
 - [8] M. K. Shin, G. M. Spinks, S. R. Shin, S. I. Kim, and S. J. Kim, Nanocomposite hydrogel with high toughness for bioactuators, *Adv. Mater.* **21**, 1712 (2009).
 - [9] N. Ogawa, M. Hashimoto, M. Takasaki, and T. Hirai, in *2009 IEEE/RSJ International Conference on Intelligent Robots and Systems* (IEEE, St. Louis, United States, 2009).
 - [10] Y. Yang, Y. Tan, X. Wang, W. An, S. Xu, W. Liao, and Y. Wang, Photothermal nanocomposite hydrogel actuator with electric-field-induced gradient and oriented structure, *ACS Appl. Mater. Interfaces* **10**, 7688 (2018).
 - [11] D. Han, C. Farino, C. Yang, T. Scott, D. Browe, W. Choi, J. W. Freeman, and H. Lee, Soft robotic manipulation and locomotion with a 3D printed electroactive hydrogel, *ACS Appl. Mater. Interfaces* **10**, 17512 (2018).
 - [12] P. M. Visakh and S. Thomas, Preparation of bionanomaterials and their polymer nanocomposites from waste and biomass, *Waste Biomass Valorization* **1**, 121 (2010).

- [13] Y. He, Moisture absorption and hygroscopic swelling behavior of an underfill material, *Thermochim. Acta* **546**, 143 (2012).
- [14] X. Liu, J. Liu, S. Lin, and X. Zhao, Hydrogel machines, *Mater. Today* **36**, 102 (2020).
- [15] J. Kim, J. W. Kim, H. C. Kim, L. Zhai, H. Ko, and R. M. Muthoka, Review of soft actuator materials, *Int. J. Precis. Eng.* **20**, 2221 (2019).
- [16] C. Laschi, B. Mazzolai, and M. Cianchetti, Soft robotics: Technologies and systems pushing the boundaries of robot abilities, *Sci. Robot.* **1**, eaah3690 (2016).
- [17] L. Hines, K. Petersen, G. Z. Lum, and M. Sitti, Soft actuators for small-scale robotics, *Adv. Mater.* **29**, 1603483 (2017).
- [18] M. T. Tolley, R. F. Shepherd, B. Mosadegh, K. C. Galloway, M. Wehner, M. Karpelson, R. J. Wood, and G. M. Whitesides, A resilient, untethered soft robot, *Soft Robot.* **1**, 213 (2014).
- [19] Z. Yang, L. Zhu, B. Li, S. Sun, Y. Chen, Y. Yan, Y. Liu, and X. Chen, Mechanical design and analysis of a crawling locomotion enabled by a laminated beam, *Extreme Mech. Lett.* **8**, 88 (2016).
- [20] M. Curatolo and P. Nardinocchi, Swelling-induced bending and pumping in homogeneous thin sheets, *J. Appl. Phys.* **124**, 085108 (2018).
- [21] J. Bae, J. Lee, S. M. Kim, J. Ha, B.-S. Lee, Y. J. Park, C. Choong, J.-B. Kim, Z. L. Wang, H.-Y. Kim, J.-J. Park, and U.-I. Chung, Flutter-driven triboelectrification for harvesting wind energy, *Nat. Commun.* **5**, 1 (2014).
- [22] S. H. Kim *et al.*, Harvesting electrical energy from carbon nanotube yarn twist, *Science* **357**, 773 (2017).
- [23] J. Xiong, H. Luo, D. Gao, X. Zhou, P. Cui, G. Thangavel, K. Parida, and P. S. Lee, Self-restoring, waterproof, tunable microstructural shape memory triboelectric nanogenerator for self-powered water temperature sensor, *Nano Energy* **61**, 584 (2019).
- [24] C. Chang, V. H. Tran, J. Wang, Y.-K. Fuh, and L. Lin, Direct-write piezoelectric polymeric nanogenerator with high energy conversion efficiency, *Nano Lett.* **10**, 726 (2010).
- [25] C. Dawson, J. F. Vincent, and A.-M. Rocca, How pine cones open, *Nature* **390**, 668 (1997).
- [26] R. Elbaum, L. Zaltzman, I. Burgert, and P. Fratzl, The role of wheat awns in the seed dispersal unit, *Science* **316**, 884 (2007).
- [27] D. Evangelista, S. Hotton, and J. Dumais, The mechanics of explosive dispersal and self-burial in the seeds of the filaree, *Erodium cicutarium* (*Geraniaceae*), *J. Exp. Biol.* **214**, 521 (2011).
- [28] J. Ha, S. M. Choi, B. Shin, M. Lee, W. Jung, and H.-Y. Kim, Hygroresponsive coiling of seed awns and soft actuators, *Extreme Mech. Lett.* **38**, 100746 (2020).
- [29] W. Jung, W. Kim, and H.-Y. Kim, Self-burial mechanics of hygroscopically responsive awns, *Integr. Comp. Biol.* **54**, 1034 (2014).
- [30] Q. Zhao, J. Dunlop, X. Qiu, F. Huang, Z. Zhang, J. Heyda, J. Dzubiella, M. Antonietti, and J. Yuan, An instant multi-responsive porous polymer actuation driven by solvent molecule sorption, *Nat. Commun.* **5**, 1 (2014).
- [31] P. Chen, Y. Xu, S. He, X. Sun, S. Pan, J. Deng, D. Chen, and H. Peng, Hierarchically arranged helical fibre actuators driven by solvents and vapours, *Nat. Nanotechnol.* **10**, 1077 (2015).
- [32] T. J. White and D. J. Broer, Programmable and adaptive mechanics with liquid crystal polymer networks and elastomers, *Nat. Mater.* **14**, 1087 (2015).
- [33] M. Behl, K. Kratz, U. Noechel, T. Sauter, and A. Lendlein, Temperature-memory polymer actuators, *Proc. Natl. Acad. Sci. U.S.A.* **110**, 12555 (2013).
- [34] S. Ha, J. Lee, K. Kim, E. J. Choi, P. Nhem, and C. Song, Anion-responsive thiourea-based gel actuator, *Chem. Mater.* **31**, 5735 (2019).
- [35] P. Basu, A. Repanas, A. Chatterjee, B. Glasmachern, U. NarendraKumar, and I. Manjubala, PEO-CMC blend nanofibers fabrication by electrospinning for soft tissue engineering applications, *Mater. Lett.* **195**, 10 (2017).
- [36] S. Timoshenko, Analysis of bi-metal thermostats, *J. Opt. Soc. Am.* **11**, 233 (1925).
- [37] B. Shin, J. Ha, M. Lee, K. Park, G. H. Park, T. H. Choi, K.-J. Cho, and H.-Y. Kim, Hygrobot: A self-locomotive ratcheted actuator powered by environmental humidity, *Sci. Robot.* **3**, eaar2629 (2018).
- [38] E. P. Gyftopoulos and G. P. Beretta, *Thermodynamics: Foundations and Applications* (Courier Corporation, New York, 2005).
- [39] P. J. Flory and J. Rehner Jr, Statistical mechanics of cross-linked polymer networks II. Swelling, *J. Chem. Phys.* **11**, 521 (1943).
- [40] S. Cai and Z. Suo, Equations of state for ideal elastomeric gels, *Europhys. Lett.* **97**, 34009 (2012).
- [41] E. Reyssat and L. Mahadevan, Hygromorphs: from pinecones to biomimetic bilayers, *J. R. Soc. Interface* **6**, 951 (2009).
- [42] X. Chen, L. Mahadevan, A. Driks, and O. Sahin, *Bacillus* spores as building blocks for stimuli-responsive materials and nanogenerators, *Nat. Nanotechnol.* **9**, 137 (2014).
- [43] R. C. P. Verpaalen, M. G. Debije, C. W. M. Bastiaansen, H. Halilovic, T. A. P. Engels, and A. P. H. J. Schenning, Programmable helical twisting in oriented humidity-responsive bilayer films generated by spray-coating of a chiral nematic liquid crystal, *J. Mater. Chem. A* **6**, 17724 (2018).
- [44] M. Dai, O. T. Picot, J. M. N. Verjans, L. T. de Haan, A. P. H. J. Schenning, T. Peijs, and C. W. M. Bastiaansen, Humidity-responsive bilayer actuators based on a liquid-crystalline polymer network, *ACS Appl. Mater. Interfaces* **5**, 4945 (2013).
- [45] J.-W. Mao, Z.-D. Chen, D.-D. Han, J.-N. Ma, Y.-L. Zhang, and H.-B. Sun, Nacre-inspired moisture-responsive graphene actuators with robustness and self-healing properties, *Nanoscale* **11**, 20614 (2019).
- [46] M. Ji, N. Jiang, J. Chang, and J. Sun, Near-infrared light-driven, highly efficient bilayer actuators based on polydopamine-modified reduced graphene oxide, *Adv. Funct. Mater.* **24**, 5412 (2014).
- [47] Y. Ma, Y. Zhang, B. Wu, W. Sun, Z. Li, and J. Sun, Polyelectrolyte multilayer films for building energetic walking devices, *Angew. Chem. Int. Ed.* **50**, 6254 (2011).
- [48] Y. Ma and J. Sun, Humido- and thermo-responsive free-standing films mimicking the petals of the morning glory flower, *Chem. Mater.* **21**, 898 (2009).

- [49] M. Rüggeberg and I. Burgert, Bio-inspired wooden actuators for large scale applications, *PLoS ONE* **10**, e0120718 (2015).
- [50] A. L. Duigou and M. Castro, Moisture-induced self-shaping flax-reinforced polypropylene biocomposite actuator, *Ind. Crops. Prod.* **71**, 1 (2015).
- [51] H.-B. Jiang, Y. Liu, J. Liu, S.-Y. Li, Y.-Y. Song, D.-D. Han, and L.-Q. Ren, Moisture-responsive graphene actuators prepared by two-beam laser interference of graphene oxide paper, *Front. Chem.* **7**, 464 (2019).
- [52] Z. Zhao, Y. Hwang, Y. Yang, T. Fan, J. Song, S. Suresh, and N.-J. Cho, Actuation and locomotion driven by moisture in paper made with natural pollen, *Proc. Natl. Acad. Sci. U.S.A.* **117**, 8711 (2020).
- [53] See Supplemental Material at <http://link.aps.org/supplemental/10.1103/PhysRevApplied.18.044061> for descriptions of the relationship between the active layer and the magnitude of mechanical work (Sec. S1); experimental validation of work ratio for our model system having various thickness of active or inactive layers (Sec. S2); detailed information of the various hygroexpansive soft actuators, which are used for comparing the work ratio (Table S1), and the abbreviations of materials (Table S2).
- [54] M. J. Harrington, K. Razghandi, F. Ditsch, L. Guiducci, M. Rüggeberg, J. W. C. Dunlop, P. Fratzl, C. Neinhuis, and I. Burgert, Origami-like unfolding of hydro-actuated ice plant seed capsules, *Nat. Commun.* **2**, 1 (2011).
- [55] A. Rafsanjani, V. Brulé, T. L. Western, and D. Pasini, Hydro-responsive curling of the resurrection plant *Selaginella lepidophylla*, *Sci. Rep.* **5**, 8064 (2015).
- [56] N. E. Stamp, Self-burial behaviour of *Erodium cicutarium* seeds, *J. Ecol.* **72**, 611 (1984).
- [57] K. Song, S.-S Chang, and S. J. Lee, How the pine seeds attach to/detach from the pine cone scale?, *Front. Life Sci.* **10**, 38 (2017).